Journal of Alloys and Compounds 1036 (2025) 181296

Contents lists available at ScienceDirect

Journal of Alloys and Compounds

journal homepage: www.elsevier.com/locate/jalcom

Thermoelectric properties of $A_{1-x}B_xIr_2Zn_{20}$ (A, B = Ce, Sm, Yb)

Benny Schundelmier [a,b], Jorge R. Galeano-Cabral [a], Ryan E. Baumbach [c], Kaya Wei [a,*]

[a] National High Magnetic Field Laboratory, Florida State University, 1800 E Paul Dirac Dr, Tallahassee, 32310, FL, USA
[b] Department of Physics, Florida State University, 77 Chieftan Way, Tallahassee, 32306, FL, USA
[c] Department of Physics, University of California, 1156 High Street, Santa Cruz, 95064, CA, USA

ARTICLE INFO

Keywords:
Thermoelectricity
Kondo lattice
Flux growth
Magnetism
Heavy fermion
Hybridization
Intermetallics
Chemical substitution

ABSTRACT

Thermoelectricity is a direct conversion between heat energy and electrical power. Thermoelectric generators provide a green approach to energy production but many materials that exhibit thermoelectric phenomena are not efficient enough to compete with other forms of renewable energy. In recent years, the 1-2-20 class of materials has displayed advanced thermoelectric properties, through large Seebeck coefficients and figures of merit. In this study, different rare earth elements were substituted in an effort to enhance the overall thermoelectric properties of these compounds. Using the molten metal flux growth technique, we synthesized crystals of $A_{1-x}B_xIr_2Zn_{20}$ (A, B = Ce, Sm, Yb). We characterized the stoichiometry using energy-dispersive x-ray spectroscopy and the structure using x-ray diffraction for each specimen. Detailed thermodynamic and electrical transport properties are investigated in order to determine the effect of chemical substitution on the rare earth site has on the thermoelectric properties.

1. Introduction

There is increasing demand for energy around the world. Hydroelectric dams, solar panels, and wind turbines are among the considered green approaches to energy production. One avenue for clean-energy production that is far less popular is thermoelectric generators. The phenomenon behind thermoelectricity is a direct conversion between heat energy and electrical power. Therefore, the voltage is produced due to a temperature differential. The source of the temperature differential would be a heat source. Many materials are inefficient at this process and, because of this, they are not widely used for electrical production. Through materials research, discovering and developing efficient thermoelectric compounds is possible [1–5].

From a practical application standpoint, one would want to find a composite system for which n-type and p-type characteristics were comparable. This means that within the same temperature regime, an n-type (electron-dominated) system and a p-type (hole-dominated) system would achieve optimal efficiency. Chemical doping and or chemical substitution studies have proven to be an instrumental aspect in the evolution of devices such as those that utilize semiconductors. Among the many examples, chemical doping studies have been demonstrated to improve the efficiency of renewable energy sources such as photovoltaics [6,7] and thermoelectrics [8,9]. For this reason, there is a compelling motivation to use this strategy to enhance known thermoelectric materials.

An attractive group for such studies are the materials with the generic formula XY_2Z_{20} (X = lanthanide or actinide, Y = transition metal, Z = Zn, Al, Cd), which are often referred to as 1-2-20 compounds. This is because these compounds form in a cubic symmetry cell setting in the Fd-3m space group, with the prototype compound being $CeCr_2Al_{20}$. The cubic unit cell provides a cage-like structure with f-block elements and transition metal elements oftentimes surrounded by a Zn, Cd, or Al framework [10]. This type of geometry has been shown to cause a "rattling"-like effect from the element trapped inside the cage, in turn reducing the thermal conductivity, this is illustrated in Fig. 1(A) [11]. A schematic view of the crystal structure is shown in Fig. 1(B), where a unit cell viewed along the a-axis is displayed. Also, important is that they often exhibit strongly correlated electronic states, from the heavy fermion properties associated with the f-element. This prompts elevated specific heat values at low temperatures and large Seebeck coefficients. Furthermore, these compounds generate intriguing physical properties such as superconductivity [12], magnetism [13], the potential for thermoelectric applications [1], and are highly tuneable (e.g., using applied pressure, magnetic fields, and chemical substitution).

Various chemical substitution studies have been implemented within the 1-2-20 group, on the rare earth site [14] and transition metal site [1,15]. Each of these studies has generated results showing that elemental substitution dramatically affects the thermoelectric properties. For example, work by Galeano-Cabral et al. on $Yb_xCe_ySm_zIr_2Zn_{20}$

* Corresponding author.
E-mail address: kwei@magnet.fsu.edu (K. Wei).

https://doi.org/10.1016/j.jallcom.2025.181296
Received 26 March 2025; Received in revised form 22 May 2025; Accepted 29 May 2025
Available online 16 June 2025

Table 1
Magnetic, lattice, and thermodynamic parameters of all specimens $A_{1-x}B_xIr_2Zn_{20}$ (A, B = Ce, Sm, Yb). μ_{eff} is the magnetic moment, θ_{CW} is the Curie–Weiss temperature, C is the Curie constant, $\chi_\circ$ is a temperature-independent term to the magnetic susceptibility, a is the lattice constant, θ_D is the Debye temperature, and θ_E is the Einstein temperature.

Sample	$\mu_{eff}(\mu_B)$	θ_{CW} (K)	C (cm^3 K/mol)	$\chi_\circ$ (cm^3/mol)	a (Å)	θ_D (K)	θ_E (K)
$CeIr_2Zn_{20}$	2.99	171.64	1.125	0	14.273	283.59	97.27
$Ce_{0.51}Sm_{0.49}Ir_2Zn_{20}$	4.06	100.5	2.066	0	14.271	293.90	101.74
$SmIr_2Zn_{20}$	0.93	88.5	0.109	0.00097	14.246	300.03	104.70
$Yb_{0.6}Ce_{0.4}Ir_2Zn_{20}$	3.5	7.51	1.539	0	14.191	307.88	102.16
$Yb_{0.57}Sm_{0.43}Ir_2Zn_{20}$	4.10	0.94	2.118	0	14.178	290.69	96.33
$YbIr_2Zn_{20}$	4.12	1.11	2.136	0	14.164	286.59	93.35

($x + y + z = 1$) shows that by introducing Yb, Ce, and Sm, the magnetic, thermal, and thermoelectric properties can be modified and improved [14]. Motivated by these works, this study focuses on chemical substitution performed on the rare earth element in $A_{1-x}B_xIr_2Zn_{20}$ (A, B = Ce, Sm, Yb). A chemical survey across the lanthanide series was performed by interchanging Ce, Sm, and Yb. We chose these elements because they allowed for a broad consideration of the f-electron state across the rare earth elements and because hybridization between f-states and conduction electron states is often a feature of these elements. Also, the differing number of f-electrons means that the types of dominant charge carriers may be distinct. Combinations of Yb-Ce, Yb-Sm, and Ce-Sm within the rare earth site were also performed. The objective of this research study is to understand what role chemical substitution on the rare earth site has on the thermoelectric performance of $A_{1-x}B_xIr_2Zn_{20}$ (A, B = Ce, Sm, Yb). We present the characterization of these materials through EDS, powder x-ray diffraction, electrical transport, heat capacity, Seebeck coefficient, and magnetometry. Comparing the physical properties of the single rare earth substitution with the double rare earth compounds can give insight into what parameters we are affecting with each substitution. Powder x-ray diffraction results indicate a contraction in the lattice constant as the composition evolves from Ce to Yb. Ce-containing compounds are primarily dominated by hole charge carriers, while Yb-containing compounds are primarily dominated by electron charge carriers. This result is demonstrated in the Seebeck data. The maximum ZT values found for Yb-containing compounds are located at low temperatures below 35 K, while Ce compounds have a maximum ZT near 100 K. This finding demonstrates the functionality of these materials over a broad range of temperatures. Partial Sm substitution in $YbIr_2Zn_{20}$ resulted in an overall enhancement in the maximum ZT value. The behavior of electronic correlations is shown to be preserved in the Yb and Ce-containing compounds and results in elevated Seebeck coefficients and ZT values.

The Mott theory for thermoelectric phenomena relates the Seebeck coefficient to the density of states at the Fermi energy by the following relation $S = \frac{2\pi^2 k_B^2 T}{3q} \frac{d \ln[N(E_F)]}{dE}$ [16]. Where S is the Seebeck coefficient and $N(E_F)$ is the density of states at the Fermi energy. In general, a higher density of states at the Fermi energy corresponds to a larger Seebeck coefficient, due to the proportionality between the two. Materials with large density of states near the Fermi energy are proposed to host superior thermoelectric properties. The compounds studied here exhibit strong hybridization between f-electrons and conduction electron states, commonly referred to as the Kondo effect [1,17]. From these correlations emerges a peak in the density of states in the electron system near the Fermi energy [18]. Consequently, the presence of hybridization propels thermoelectric performance in these compounds.

2. Experimental methods

Intermetallic crystals of $A_{1-x}B_xIr_2Zn_{20}$ (A, B = Ce, Sm, Yb) were synthesized using the molten metallic flux growth technique via a composition of Zinc self flux [19,20]. The starting elements were greater than 99.9% purity. Elements were combined in the atomic ratios of (Yb, Sm, Ce):Ir:Zn = 1:2:60, loaded into 2-ml alumina Canfield crucibles, and sealed under vacuum in quartz tubes [21]. The ampules were pumped and purged five times using argon gas and sealed at nearly 30 millitorr. The quartz tubes were placed in a resistive box furnace and then heated to 1050 °C at a rate of 50 °C/h. Specimens were held at 1050 °C for 72 h, cooled to 700 °C at a rate of 2 °C/hour, and then held at 700 °C for 48 h. At this temperature, the quartz tubes were removed from the furnace and centrifuged to separate the remaining Zinc self flux from the precipitated crystals. The specific process of centrifugation for each sample was a spin time exceeding 30 s at the maximum speed of the centrifuge, approximately 7000 revolutions per minute. Properties of $YbIr_2Zn_{20}$ and $Yb_{0.6}Ce_{0.4}Ir_2Zn_{20}$ are from previous reports [1,14].

The crystallographic structure was characterized by powder x-ray diffraction using a Rigaku SmartLab SE x-ray diffractometer with a Cu Kα source. The details of the structural analysis are listed in Table 1. Energy-dispersive x-ray spectroscopy (EDS) was performed using an FEI NOVA 400 nanoSEM scanning electron microscope. The Nova NanoSEM is an ultra-high-resolution Low-Vacuum Schottky Field-Emission Scanning Electron Microscope (FEG-SEM). The system provides energy-dispersive x-ray spectroscopy (EDS or EDX) capabilities using an Oxford 100 mm^2 UltimMax SDD (silicon drift detector) x-ray detector elemental composition.

Magnetometry of all samples was gathered using Quantum Design VSM Magnetic Property Measurement System (MPMS). Crystalline samples were mounted to a quartz rod using GE varnish. Magnetic susceptibility measurements were performed at a constant applied magnetic field of H = 0.1 T while sweeping temperatures from 1.8 K to 300 K. Zero field-cooled and field-cooled measurements were conducted. Magnetization measurements were performed at a constant temperature of 1.8 K while sweeping the magnetic field between −7 T and 7 T.

Thermal transport properties were measured using the 4He option in the Quantum Design Physical Property Measurement System. The Thermal Transport Option (TTO) was used to simultaneously measure the sample's thermal conductivity, Seebeck coefficient, and electrical resistivity. The samples were prepared by cutting a crystalline specimen into a bar shape using a wire saw. The sample was then polished using 5-micron diamond paper. Using silver epoxy, leads were adhered to the sample and cured in a 150 °C furnace for a minimum of five minutes. The measurements were carried out from T = 1.8 K to 400 K.

Heat capacity (C_p) was performed using the 4He option in the PPMS. The software-automated addenda measurement for background subtraction was performed by applying a small amount of Apiezon N grease to the HC puck. Then, the sample was placed on the Apiezon N grease as an adhesive to thermally sync the sample to the sample platform. The measurements were performed at a temperature range from T = 1.8 K to 250 K in zero magnetic field.

3. Results and discussion

EDS was performed to determine the elemental composition. The average EDS results over multiple spectra were used to determine the labeled stoichiometry. From the average EDS results it was determined that we produced $YbIr_2Zn_{20}$, $CeIr_2Zn_{20}$, $SmIr_2Zn_{20}$, $Yb_{0.57}Sm_{0.43}Ir_2Zn_{20}$, $Yb_{0.6}Ce_{0.4}Ir_2Zn_{20}$, and $Ce_{0.51}Sm_{0.49}Ir_2Zn_{20}$.

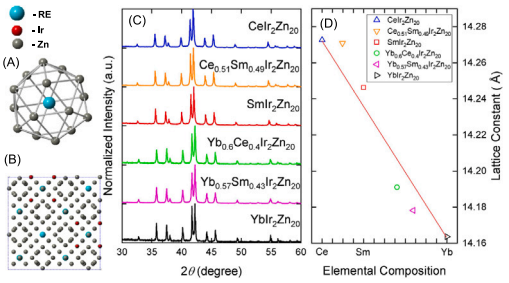

Fig. 1. (A) Frank–Kasper polyhedron formed by *RE* (*RE* = Rare Earth) encapsulated by Zn atoms. (B) *a*-axis directional view of the unit cell of $RE\mathrm{Ir_2Zn_{20}}$. (C) Powder x-ray diffraction data for $A_{1-x}B_x\mathrm{Ir_2Zn_{20}}$ (*A*, *B* = Ce, Sm, Yb). The diffraction patterns have been intensity normalized and shifted vertically for transparency. (D) The elemental composition is shown on the x-axis and the lattice constant in angstroms is shown on the y-axis for all compounds.

Powder x-ray diffraction of the specimens was performed on $A_{1-x}B_x\mathrm{Ir_2Zn_{20}}$ (*A*, *B* = Ce, Sm, Yb). Fig. 1(A) is a comparison of the diffraction patterns. It is apparent that all peaks align through the collected 2θ regime, indicating that all samples are of the expected crystalline structure. A Rietveld refinement was performed on each diffraction pattern to determine the lattice constant of the individual specimens. The lattice constant versus the elemental composition of all compounds is plotted in Fig. 1(B). Based on the comparison, there is a systematic reduction in the lattice constant from Ce to Yb. This is consistent with a lanthanide contraction which is expected in a chemical substitution series [22–26]. The lattice constant of each compound is listed in Table 1.

Temperature-dependent electrical resistivity $\rho(T)$ for all samples $A_{1-x}B_x\mathrm{Ir_2Zn_{20}}$ (*A*, *B* = Ce, Sm, Yb) are shown in Fig. 2(A). In the $\rho(T)$ of $\mathrm{YbIr_2Zn_{20}}$ at temperatures below 25 K there is an arch and above 25 K there is a linear trend. The arch was previously discussed as evidence for the Kondo lattice behavior [27]. Normal metallic behavior with a slight curvature at lower temperatures is shown in $\mathrm{SmIr_2Zn_{20}}$, which agrees with former reports of this compound [28]. The overall $\rho(T)$ of this sample is much lower than the counterparts, indicating simple, weakly correlated electron metallic behavior. The curvature of the $\rho(T)$ for $\mathrm{CeIr_2Zn_{20}}$ is much different in comparison to $\mathrm{YbIr_2Zn_{20}}$ and $\mathrm{SmIr_2Zn_{20}}$. At low temperatures, $\rho(T)$ increases quadratically with increasing temperature, then around 100 K there is an inflection point where $\rho(T)$ starts to saturate. Finally, a weak linear increase is seen above 250 K. This shoulder-type feature resembles a Kondo lattice-type signature, as shown in many Ce-containing intermetallics [29,30]. The comparison between the overall trend in $\rho(T)$ from $\mathrm{YbIr_2Zn_{20}}$ and $\mathrm{Yb_{0.57}Sm_{0.43}Ir_2Zn_{20}}$ show similar traits. The overall $\rho(T)$ is about 25μΩ-cm smaller in $\mathrm{Yb_{0.57}Sm_{0.43}Ir_2Zn_{20}}$ and the low-temperature hump is shifted to lower temperatures. The $\rho(T)$ of $\mathrm{Yb_{0.6}Ce_{0.4}Ir_2Zn_{20}}$ is slightly quadratic at low temperatures and tapers off to linear with increasing temperature. $\mathrm{Ce_{0.51}Sm_{0.49}Ir_2Zn_{20}}$ has a very broad arch across the temperature range that mimics an average over its two parent compounds, $\mathrm{CeIr_2Zn_{20}}$ and $\mathrm{SmIr_2Zn_{20}}$.

Temperature-dependent $S(T)$ of all compounds $A_{1-x}B_x\mathrm{Ir_2Zn_{20}}$ (*A*, *B* = Ce, Sm, Yb) are summarized in Fig. 2(B). As previously reported, $\mathrm{YbIr_2Zn_{20}}$ has a large negative $S(T)$ attributed to the primary charge carriers being electrons with a maximum value near 25 K [1]. The large values are associated with Kondo lattice hybridization. $\mathrm{SmIr_2Zn_{20}}$ has a low and broad positive $S(T)$, that is negligible compared to its counterparts. This is consistent with the electrical resistivity measurements that indicate simple metallic behavior. The positive $S(T)$ throughout the measured temperature range is a reflection of the primary charge carriers being holes in this compound. $\mathrm{CeIr_2Zn_{20}}$ has a sizable positive value justified by hole charge carrier characteristics with a maximum value close to 90 K, consistent with the observation of Kondo lattice behavior in $\rho(T)$. Although the curvature is consistent with previous

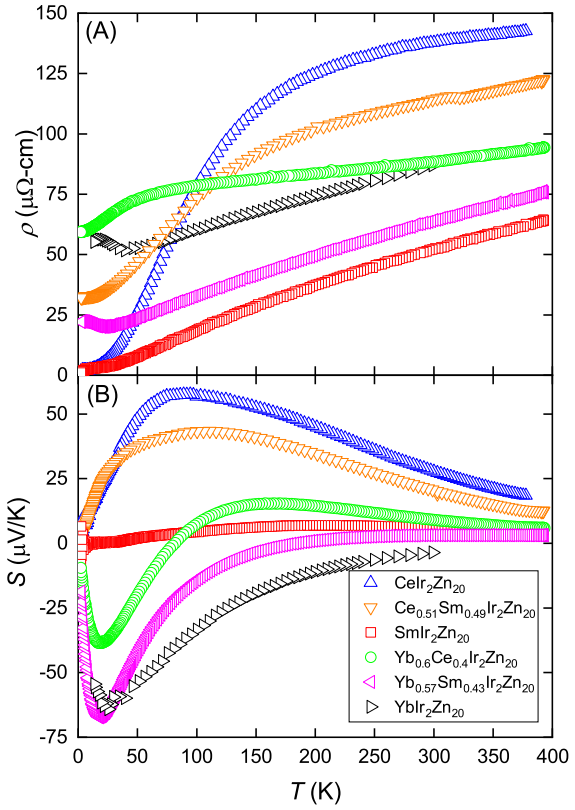

Fig. 2. (A) Temperature-dependent electrical resistivity $\rho(T)$ and (B) temperature-dependent Seebeck coefficient $S(T)$ for $A_{1-x}B_x\mathrm{Ir_2Zn_{20}}$ (*A*, *B* = Ce, Sm, Yb).

reports, the maximum Seebeck we observe for $\mathrm{CeIr_2Zn_{20}}$ is significantly higher in contrast [31]. Comparing $\mathrm{YbIr_2Zn_{20}}$ and $\mathrm{Yb_{0.57}Sm_{0.43}Ir_2Zn_{20}}$ both display negative $S(T)$ with a maximum value close 25 K, but there is a slight enhancement in the overall trend with the addition of Sm. The $\mathrm{Yb_{0.6}Ce_{0.4}Ir_2Zn_{20}}$ takes after the two parent compounds $\mathrm{YbIr_2Zn_{20}}$ and $\mathrm{CeIr_2Zn_{20}}$, where the trend transitions from a negative to a positive value with increasing temperature. This demonstrates a competition between the dominant charge carriers in this compound. There is a major resemblance between the Seebeck curves for $\mathrm{CeIr_2Zn_{20}}$ and $\mathrm{Ce_{0.51}Sm_{0.49}Ir_2Zn_{20}}$. Both have a positive $S(T)$ with a maximum value near 90 K, although there is a significant reduction in the overall trend with the addition of Sm.

The screening effect connected to the Kondo interaction between local *f*-moments and conduction electrons has been established to cause regions of non-linearity in electrical resistivity. The Kondo effect has been shown to generate local maxima and logarithmic type decreases in electrical resistivity verse temperature curves [17,27,32]. The $\rho(T)$ for all samples excluding $\mathrm{SmIr_2Zn_{20}}$ contain a feature resembling the type of curvature found in Kondo lattice systems. The scattering mechanisms are different for the Yb-containing compounds compared to the Ce-containing compounds, leading to the differing $\rho(T)$ for the various chemical substitutions studied here.

Comparing Fig. 2(A) and (B) it is clear that the Kondo coherence temperature in the Ce and Yb-containing compounds are consistent. Meaning that the curvature features shown in the resistivity correlate with the maximum in Seebeck coefficient. While $\mathrm{SmIr_2Zn_{20}}$ shows metallic behavior in both resistivity and Seebeck. This advocates that electronic correlations are the driving force for enhanced Seebeck coefficients in the Ce and Yb-containing compounds.

Temperature-dependent magnetic susceptibility $\chi(T)$ of all compounds $A_{1-x}B_x\mathrm{Ir_2Zn_{20}}$ (*A*, *B* = Ce, Sm, Yb) are shown in Fig. 3(A). All $\chi(T)$ data was collected in a constant magnetic field of 0.1 T. The $\chi(T)$

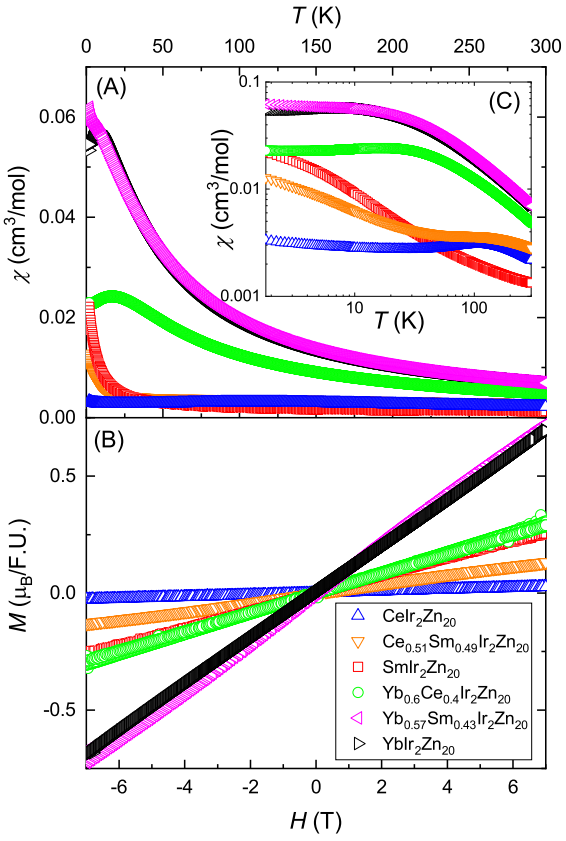

Fig. 3. Temperature-dependent (A) magnetic susceptibility $\chi(T)$, (B) field dependent magnetization $M(H)$, and (C) $log_{10}(\chi)(log_{10}(T))$ for $A_{1-x}B_xIr_2Zn_{20}$ (A, B = Ce, Sm, Yb). All $M(H)$ curves were collected at a temperature of 1.8 K and all $\chi(T)$ data was collected at 0.1 T.

of $YbIr_2Zn_{20}$ and $Yb_{0.57}Sm_{0.43}Ir_2Zn_{20}$ are nearly identical at temperatures above 5 K. There is a significant down turn for $YbIr_2Zn_{20}$ below 5 K, this is consistent with previous reports on this compound [1]. The addition of Sm in $YbIr_2Zn_{20}$ causes a significant upturn at 5 K that indicates enhanced spin susceptibility. Similar behavior is seen in $SmIr_2Zn_{20}$, which has been proposed to exhibit Van Vleck paramagnetism that originates from the Sm μ_{eff}-electron states. There is a slight curvature over the measured temperature range, and near 50 K there is an outstanding upturn. These features comply with past reports of this compound [28]. Complex magnetic behaviors such as those shown here are often seen in Samarium containing systems [33–35]. $CeIr_2Zn_{20}$ has a weak overall moment compared to the other compounds listed. A broad hump over the 25 K to 250 K temperature regime and a subtle upturn near 5 K suggests a temperature-dependent intermediate valence system. This behavior is consistent with previous reports on this compound [31]. Curie–Weiss type behavior is shown in $Yb_{0.6}Ce_{0.4}Ir_2Zn_{20}$ above 25 K and has a rounded downturn below 25 K. This behavior demonstrates a mixture of the features shown by its parent compounds. $Ce_{0.51}Sm_{0.49}Ir_2Zn_{20}$ also takes after its parent compounds; There is a slight curve above 25 K and a strong upturn at low temperatures. The details of these features can be distinguished in the inset of Fig. 3(C). A Curie–Weiss fit was applied to the magnetic susceptibility data for each sample using the following equation [36]

$$\chi = \frac{C}{T - \theta_{CW}} - \chi_o. \tag{1}$$

where C is the Curie constant, T is the temperature, χ_o is a temperature-independent term, and θ_{CW} is the Curie temperature. Fit results are summarized in Table 1. The most convenient method for fitting Curie–Weiss to $\chi(T)$ is by plotting $1/\chi$ vs. T. The linear regime correlates to the paramagnetic state, the slope and intercepts of the linear regime correspond to the $1/C$ and θ_{CW}/C, respectively. The effective magnetic moment can be calculated using the following equation, $\mu_{eff} = 2.82\sqrt{\frac{C}{n}}$. θ_{CW} is calculated using the slope divided by C [36].

The results of the calculated effective magnetic moments (μ_{eff}) of $YbIr_2Zn_{20}$ is 4.12 (μ_B), this is comparable to the expected theoretical value of Yb 3+ which is 4.53 (μ_B) [37]. The calculated μ_{eff} of $CeIr_2Zn_{20}$ is 2.99 (μ_B), compared to the expected theoretical value of Ce 3+ 2.54 (μ_B), the overestimation is attributed to the intermediate valence behavior that persist below 100 K [37]. The intermediate valence behavior established in this compound means that the oxidation state is fluctuating between Ce 3+ and Ce 4+, this mixed state is dependent upon temperature and results in a shift in equilibrium. This results in a partially paramagnetic state in the measured temperature range which leads to an approximated Curie–Weiss fit. Including an associated χ_o term of 0.00097 (cm^3/mol), the calculated μ_{eff} of $SmIr_2Zn_{20}$ is 0.93 (μ_B), compared to the theoretical value of Sm 3+ 0.85 (μ_B) [37]. For similar reasons as described for the valence of Ce, the Curie–Weiss fit for Sm results in an over approximation for μ_B. The μ_{eff} from $Yb_{0.57}Sm_{0.43}Ir_2Zn_{20}$ is 4.10 (μ_B), meaning that the effective moment is primarily dominated by Yb magnetism in this compound. $Yb_{0.6}Ce_{0.4}Ir_2Zn_{20}$ has a μ_{eff} of 3.5 (μ_B), which is approximately an average over the μ_{eff} from the two parent compounds. The μ_{eff} from $Ce_{0.51}Sm_{0.49}Ir_2Zn_{20}$ is 4.06 (μ_B), which signifies the magnetic intricacy associated to the combination of Sm and Ce magnetism.

The Curie–Weiss temperature (θ_{CW}) of all compounds generally follows a systematic trend. The θ_{CW} is smallest in Yb-containing compounds and highest in Ce-containing compounds. This is evident based on the shape of the magnetic susceptibility curves seen in the inset of Fig. 3(C). The fact that the Ce-containing compounds results in larger θ_{CW} compared to the Yb and Sm-containing compounds, indicates that the correlation strength between ions is highest in the Ce compounds. θ_{CW} of all compounds are positive indicating that there is net ferromagnetic interactions between spins.

Field-dependent $M(H)$ of all compounds $A_{1-x}B_xIr_2Zn_{20}$ (A, B = Ce, Sm, Yb) are displayed in Fig. 3(B). The $M(H)$ for all compounds have a positive linear relationship with increasing slope. $Yb_{0.57}Sm_{0.43}Ir_2Zn_{20}$ has a subtle S-shaped curvature resembling a slight ferromagnet feature. The magnitude of $M(H)$ depends on the substitution. Generally the magnitude increases from Ce to Yb concentrations. This is consistent with the $\chi(T)$ data. There are no signs of saturation in the magnetic moment for any sample in magnetic fields up to 7 T. This implies that each sample exhibits a paramagnetic response across the measured field range and temperature.

Temperature-dependent heat capacity data $C_p(T)$ for all samples $A_{1-x}B_xIr_2Zn_{20}$ (A, B = Ce, Sm, Yb) are presented in Fig. 4. As expected, the curvature of all samples above 10 K is nearly identical, representing the phonon contribution to $C_p(T)$. All samples were fit to the Debye Einstein model using the following equation [38]

$$C_p(T) = C_D\left(\frac{T}{\theta_D}\right)^3 \int_0^{\theta_D/T} \frac{x^4 e^x}{(e^x-1)^2} dx + C_E\left(\frac{\theta_E}{T}\right)^2 \frac{e^{\theta_E/T}}{(e^{\theta_E/T}-1)^2}. \tag{2}$$

The Einstein temperature (θ_E) and the Debye temperature (θ_D) were extrapolated from the fit. This information is summarized in Table 1. Considering that there is practically no variation in the Debye temperature across all samples, it is evident that the substitution of the rare earth site has little effect on the lattice behavior. The slight wiggling at temperatures above 200 K shown by some of the data is attributed to the Apiezon N grease [39], but does not hinder the nature of the sample data.

The overall trend of $C_p/T(T^2)$ for $CeIr_2Zn_{20}$ and $Yb_{0.6}Ce_{0.4}Ir_2Zn_{20}$ are representative of a nonmagnetic metal. There is no evidence of a first-order or second-order phase transition at low temperatures in these samples. There is a low-temperature feature shown for the $YbIr_2Zn_{20}$

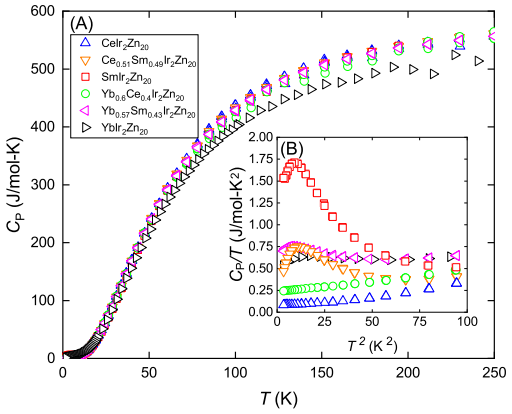

Fig. 4. Temperature-dependent (A) heat capacity $C_p(T)$ and (B) heat capacity divided by temperature versus temperature squared $C_p/T(T^2)$ for $A_{1-x}B_xIr_2Zn_{20}$ (A, B = Ce, Sm, Yb).

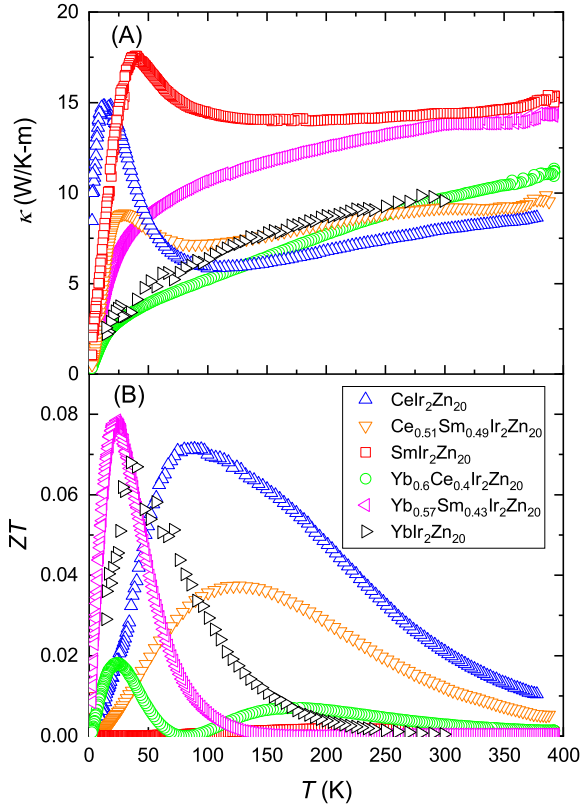

Fig. 5. (A) Temperature-dependent thermal conductivity $\kappa(T)$ and (B) temperature-dependent thermoelectric figure of merit ZT for $A_{1-x}B_xIr_2Zn_{20}$ (A, B = Ce, Sm, Yb).

and $SmIr_2Zn_{20}$ data. All Sm-containing compounds possess a revealing low-temperature ascent. This characteristic indicates that there is some additional entropy that could be associated with magnetic entropy [33], crystal electric field splitting [40], etc. The elevated low-temperature specific heat shown by all compounds gives some insight as to why they exhibit enriched Seebeck coefficients. However, the additional entropy discussed is assumed to be hiding the pure electronic contribution to the specific heat. This is likely the reason that there is not a systematic trend associated with the magnitude of low-temperature specific heat and Seebeck coefficient values.

Temperature-dependent thermal conductivity $\kappa(T)$ is shown in Fig. 5(A). $CeIr_2Zn_{20}$, $SmIr_2Zn_{20}$, and $Ce_{0.51}Sm_{0.49}Ir_2Zn_{20}$ has a strong elevation at low temperatures below 100 K. A broad arch at temperatures blow 100 K is present in $YbIr_2Zn_{20}$, $Yb_{0.6}Ce_{0.4}Ir_2Zn_{20}$, and $Yb_{0.57}Sm_{0.43}Ir_2Zn_{20}$. Above 100 K, all samples exhibit linearly increasing $\kappa(T)$ with increasing temperature. Corrections were made to the thermal conductivity to account for radiation loss. This correction was performed following the method illustrated in Pope et al. [41].

Temperature-dependent thermoelectric figure of merit ZT for $A_{1-x}B_xIr_2Zn_{20}$ (A, B = Ce, Sm, Yb) is shown in Fig. 5 (b). The overall ZT is a reflection of the $S(T)$ data. This is due to the fact that the dominant term in the ZT is $S(T)$. $Yb_{0.57}Sm_{0.43}Ir_2Zn_{20}$, $CeIr_2Zn_{20}$, and $YbIr_2Zn_{20}$ have the highest ZT values, respectively. There are two peaks present in $Yb_{0.6}Ce_{0.4}Ir_2Zn_{20}$, one is located at a temperature near the max ZT value of $CeIr_2Zn_{20}$ and the other near the max value of $YbIr_2Zn_{20}$. The maximum ZT in $Ce_{0.51}Sm_{0.49}Ir_2Zn_{20}$ is reduced to roughly half of the value of the pure Ce counterpart. $SmIr_2Zn_{20}$ has a negligible ZT compared to these compounds. The addition of Ce in the rare earth site of this group has been shown to push the maximal ZT value to higher temperatures.

4. Conclusion

We have successfully produced single-crystalline samples of $A_{1-x}B_xIr_2Zn_{20}$ (A, B = Ce, Sm, Yb) as a chemical substitution series on the rare earth site. Our study of exchanging rare earth elements shows that the physical properties can be modified accordingly. The addition of Sm in $YbIr_2Zn_{20}$, that being $Yb_{0.57}Sm_{0.43}Ir_2Zn_{20}$, leads to an enhancement in the ZT by nearly 13%, the maximum ZT of $Yb_{0.57}Sm_{0.43}Ir_2Zn_{20}$ is 0.078 at 23.4 K compared to 0.068 at 34.6 K for $YbIr_2Zn_{20}$. There is a dramatic difference in the behaviors of $S(T)$ in $YbIr_2Zn_{20}$, $SmIr_2Zn_{20}$, and $CeIr_2Zn_{20}$. The $CeIr_2Zn_{20}$ has a positive overall peak indicating that the dominant charge carriers are holes. In contrast, for $YbIr_2Zn_{20}$ the dominant charge carriers are electrons. Since both n-type and p-type thermometric materials are needed to construct thermoelectric modules, the fact that these two compounds are similar in composition could be a great advantage for improving the lifetime of the modules. The maximal ZT value has a shift in temperature that depends on the concentration of x in $A_{1-x}B_xIr_2Zn_{20}$ (A, B = Ce, Sm, Yb). This study demonstrates that rare earth substitution is a control for the tunability of temperature efficiency, which is an important consideration for device design. The $S(T)$ of $SmIr_2Zn_{20}$ is primarily negligible over the measured temperature range. We find that the $S(T)$ for $Yb_{0.6}Ce_{0.4}Ir_2Zn_{20}$ and $Ce_{0.51}Sm_{0.49}Ir_2Zn_{20}$ is nearly an average over the two parent compounds. When substituting with Sm, for instance in $Yb_{0.57}Sm_{0.43}Ir_2Zn_{20}$, the $S(T)$ values are enhanced. This finding is quite remarkable since the $S(T)$ of $SmIr_2Zn_{20}$ alone is insignificant. The shape of the resistivity curves indicates that hybridization is preserved when substituting the rare earth site with Yb and Ce. The hybridization energy scale is consistent when comparing the $\rho(T)$ and $S(T)$ for all compounds except for $SmIr_2Zn_{20}$, which displays a normal metallic behavior. These features indicate that appreciable hybridization strength between the f-states and conduction electrons could be the driving force behind the enhanced $S(T)$.

One limitation that effectively restrains the ZT values in these compounds is the high thermal conductivity. To further enhance the thermoelectric properties in these compounds, one approach is to increase grain boundary scatterings to reduce the lattice thermal conductivity. High density poly crystals comprised of these materials should affect the thermal conductivity and result in an overall higher figure of merit. Chemical substitutions using other rare earth elements or additional combinations could be a useful avenue to further modulate the thermoelectric properties in this group of compounds. Although, the authors would like to mention that targeting a specific concentration of any particular element can be challenging and is a limiting factor when performing a substitution series study such as the one described here. The motive of cryogen-free refrigeration in applications for materials

science and engineering is evident. Although, in general, thermoelectric refrigeration has lower efficiency than conventional refrigeration systems, its unique characteristics (for example, no moving parts, long lifetime, and easily sizable) make it a strong candidate for this particular application. The materials reported here have a maximum efficiency below the boiling point of liquid nitrogen, and therefore have the potential to be implemented in a cryogen-free refrigeration device.

CRediT authorship contribution statement

Benny Schundelmier: Writing – review & editing, Writing – original draft, Visualization, Validation, Methodology, Investigation, Formal analysis, Data curation, Conceptualization. **Jorge R. Galeano-Cabral:** Writing – review & editing, Data curation. **Ryan E. Baumbach:** Writing – review & editing. **Kaya Wei:** Writing – review & editing, Writing – original draft, Supervision, Resources, Project administration, Funding acquisition, Conceptualization.

Declaration of competing interest

The authors declare that they have no known competing financial interests or personal relationships that could have appeared to influence the work reported in this paper.

Acknowledgments

The National High Magnetic Field Laboratory is supported by the National Science Foundation, United States through NSF/DMR-2128556/DMR-1644779 and the State of Florida. Benny Schundelmier and Kaya Wei acknowledge the support of the NHMFL User Collaboration Grant Program (UCGP). Ryan E. Baumbach acknowledges support from startup funds provided by the University of California, Santa Cruz.

References

[1] Kaya Wei, Jennifer N Neu, You Lai, Kuan-Wen Chen, Dean Hobbis, George S Nolas, David E Graf, Theo Siegrist, Ryan E Baumbach, Enhanced thermoelectric performance of heavy-fermion compounds $YbTM_2Zn_{20}$ (TM=Co, Rh, Ir) at low temperatures, Sci. Adv. 5 (5) (2019) eaaw6183.

[2] Hayati Mamur, M.R.A. Bhuiyan, Fatih Korkmaz, Mustafa Nil, A review on bismuth telluride (bi_2te_3) nanostructure for thermoelectric applications, Renew. Sustain. Energy Rev. 82 (2018) 4159–4169.

[3] Xiao-Lei Shi, Jin Zou, Zhi-Gang Chen, Advanced thermoelectric design: from materials and structures to devices, Chem. Rev. 120 (15) (2020) 7399–7515.

[4] G.S. Nolas, D.T. Morelli, Terry M. Tritt, Skutterudites: A phonon-glass-electron crystal approach to advanced thermoelectric energy conversion applications, Annu. Rev. Mater. Sci. 29 (1) (1999) 89–116.

[5] GSn Nolas, J.L. Cohn, G.A. Slack, S.B. Schujman, Semiconducting ge clathrates: Promising candidates for thermoelectric applications, Appl. Phys. Lett. 73 (2) (1998) 178–180.

[6] Mahmoud S Alkathy, Fabio L Zabotto, Flavio Paulo Milton, JA Eiras, Bandgap tuning in samarium-modified bismuth titanate by site engineering using iron and cobalt co-doping for photovoltaic application, J. Alloys Compd. 908 (2022) 164222.

[7] Calvin K. Chan, Wei Zhao, Antoine Kahn, Ian G. Hill, Influence of chemical doping on the performance of organic photovoltaic cells, Appl. Phys. Lett. 94 (20) (2009).

[8] Jian Liu, Bas van der Zee, Riccardo Alessandri, Selim Sami, Jingjin Dong, Mohamad I Nugraha, Alex J Barker, Sylvia Rousseva, Li Qiu, Xinkai Qiu, et al., N-type organic thermoelectrics: demonstration of ZT > 0.3, Nat. Commun. 11 (1) (2020) 5694.

[9] Niraj Kumar Singh, Sivaiah Bathula, Bhasker Gahtori, Kriti Tyagi, D Haranath, Ajay Dhar, The effect of doping on thermoelectric performance of p-type SnSe: Promising thermoelectric material, J. Alloys Compd. 668 (2016) 152–158.

[10] Tono Nasch, Wolfgang Jeitschko, Ute Ch Rodewald, Ternary rare earth transition metal zinc compounds RT2Zn20 with T=Fe, Ru, Co, Rh, and Ni, Z. Naturforschung B 52 (9) (1997) 1023–1030.

[11] C.E. Ekuma, Thermal transport in Yb-based 1-2-20 materials, Europhys. Lett. 145 (4) (2024) 46002.

[12] M.J. Winiarski, B. Wiendlocha, M. Sternik, P. Wiśniewski, J.R. O'Brien, D. Kaczorowski, T. Klimczuk, Rattling-enhanced superconductivity in MV_2Al_{20} (M = Sc, Lu, Y) intermetallic cage compounds, Phys. Rev. B 93 (2016) 134507, URL https://link.aps.org/doi/10.1103/PhysRevB.93.134507.

[13] P. Swatek, M. Daszkiewicz, D. Kaczorowski, Paramagnetic heavy-fermion ground state in single-crystalline UIr_2Zn_{20}, Phys. Rev. B 85 (2012) 094426, URL https://link.aps.org/doi/10.1103/PhysRevB.85.094426.

[14] Jorge R Galeano-Cabral, Eliana Karr, Benny Schundelmier, Olatunde Oladehin, Eun S Choi, Theo Siegrist, Juan Ordonez, Sarvjit Shastri, Valeri Petkov, Ryan E Baumbach, et al., Enhanced thermoelectric properties of heavy-fermion compounds $Yb_xCe_ySm_z$ Ir 2 Zn 20 (x+ y+ z=1), Phys. Rev. Mater. 7 (2) (2023) 025406.

[15] Jorge R Galeano-Cabral, Benny Schundelmier, Olatunde Oladehin, Keke Feng, Juan C Ordonez, Ryan E Baumbach, Kaya Wei, Effect of Ni doping on the thermoelectric properties of YbCo2Zn20, Materials 17 (8) (2024) 1906.

[16] Faiz Salleh, Hiroya Ikeda, Seebeck coefficient of heavily p-doped si calculated from an alteration in electronic density of states, J. Electron. Mater. 40 (2011) 903–906.

[17] E.D. Mun, S. Jia, S.L. Bud'ko, P.C. Canfield, Thermoelectric power of the YbT_2Zn_{20} (T = Fe, Ru, Os, Ir, Rh, and Co) heavy fermions, Phys. Rev. B 86 (2012) 115110, URL https://link.aps.org/doi/10.1103/PhysRevB.86.115110.

[18] Po-Chen Kuo, Neill Lambert, Mauro Cirio, Yi-Te Huang, Franco Nori, Yueh-Nan Chen, Kondo QED: The kondo effect and photon trapping in a two-impurity Anderson model ultrastrongly coupled to light, Phys. Rev. Res. 5 (2023) 043177, URL https://link.aps.org/doi/10.1103/PhysRevResearch.5.043177.

[19] MS Torikachvili, S Jia, Eun Deok Mun, ST Hannahs, RC Black, WK Neils, Dinesh Martien, Sergey L Bud'ko, PC Canfield, Six closely related YbT_2Zn_{20} (T = Fe, Co, Ru, Rh, Os, Ir) heavy fermion compounds with large local moment degeneracy, Proc. Natl. Acad. Sci. 104 (24) (2007) 9960–9963.

[20] Shuang Jia, Ni Ni, Sergey L. Bud'ko, P.C. Canfield, Magnetic properties of $Gd_xY_{1-x}Fe_2Zn_{20}$: Dilute, large-S moments in a nearly ferromagnetic Fermi liquid, Phys. Rev. B—Condens. Matter Mater. Phys. 76 (18) (2007) 184410.

[21] Paul C Canfield, Tai Kong, Udhara S Kaluarachchi, Na Hyun Jo, Use of frit-disc crucibles for routine and exploratory solution growth of single crystalline samples, Phil. Mag. 96 (1) (2016) 84–92.

[22] Bodie E. Douglas, The lanthanide contraction, J. Chem. Educ. 31 (11) (1954) 598.

[23] Amy-Jayne Hutchings, Fatemah Habib, Rebecca J Holmberg, Ilia Korobkov, Muralee Murugesu, Structural rearrangement through lanthanide contraction in dinuclear complexes, Inorg. Chem. 53 (4) (2014) 2102–2112.

[24] Robert D. Shannon, Revised effective ionic radii and systematic studies of interatomic distances in halides and chalcogenides, Found. Crystallogr. 32 (5) (1976) 751–767.

[25] Robert B. Jordan, Lanthanide contraction: What is normal? Inorg. Chem. 62 (9) (2023) 3715–3721.

[26] Robert B. Jordan, The lanthanide contraction: What is an abnormal and why? Inorg. Chem. (2025).

[27] M. Lavagna, Claudine Lacroix, Michel Cyrot, Resistivity of the Kondo lattice, J. Phys. F: Met. Phys. 12 (4) (1982) 745.

[28] Yuki Taga, Kiyohiro Sugiyama, Kentaro Enoki, Yusuke Hirose, Ken Iwakawa, Akinobu Mori, Kazuhiro Ishida, Tetsuya Takeuchi, Masayuki Hagiwara, Koichi Kindo, et al., Magnetic properties of RIr_2Zn_{20} (R: rare earth) with the caged structure, J. Phys. Soc. Japan 81 (Suppl. B) (2012) SB051.

[29] D. Kaczorowski, A. Ślebarski, Kondo lattice behavior and magnetic ordering in $CeRh_2Si$, Phys. Rev. B 81 (2010) 214411, URL https://link.aps.org/doi/10.1103/PhysRevB.81.214411.

[30] A. Kowalczyk, V.H. Tran, T. Toliński, W. Miiller, Electrical resistivity and thermoelectric power of the Kondo lattice $CeNiAl_4$, Solid State Commun. (ISSN: 0038-1098) 144 (5) (2007) 185–188, URL https://www.sciencedirect.com/science/article/pii/S0038109807006187.

[31] P. Swatek, D. Kaczorowski, Intermediate valence behavior in the novel cage compound $CeIr_2Zn_{20}$, J. Phys.: Condens. Matter. 25 (5) (2013) 055602.

[32] Hidenori Miyagawa, Gendo Oomi, Masashi Ohashi, Isamu Satoh, Takemi Komatsubara, Masato Hedo, Yoshiya Uwatoko, Electronic states of single crystal CeAl 2 near the pressure-induced quantum critical point, Phys. Rev. B—Condens. Matter Mater. Phys. 78 (6) (2008) 064403.

[33] Keke Feng, Caleb Bush, Olatunde Oladehin, Minhyea Lee, Ryan Baumbach, Complex antiferromagnetic order in the metallic triangular lattice compound Sm_4Ge_2, Phys. Rev. B 109 (1) (2024) 014436.

[34] J. Pospíšil, M. Kratochvílová, J Prokleška, M Diviš, V Sechovskỳ, Samarium magnetism studied on $SmPd_2Al_3$ single crystal, Phys. Rev. B—Condens. Matter Mater. Phys. 81 (2) (2010) 024413.

[35] K.A. McEwen, P.F. Touborg, G.J. Cock, L.W. Roeland, Magnetic properties of samarium, J. Phys. F: Met. Phys. 4 (12) (1974) 2264.

[36] Stephen Blundell, Magnetism in Condensed Matter, OUP Oxford, 2001.

[37] Stephen Elliott, The Physics and Chemistry of Solids, John Wiley & Sons, 1998.

[38] T Besara, D Ramirez, J Sun, JB Whalen, TD Tokumoto, SA McGill, DJ Singh, T Siegrist, Ba_2TeO: A new layered oxytelluride, J. Solid State Chem. 222 (2015) 60–65.

[39] W. Schnelle, J. Engelhardt, E. Gmelin, Specific heat capacity of Apiezon N high vacuum grease and of Duran borosilicate glass, Cryogenics 39 (3) (1999) 271–275.

[40] William M Yuhasz, Neil A Frederick, P-C Ho, NP Butch, BJ Taylor, TA Sayles, M Brian Maple, Jonathan B Betts, AH Lacerda, P Rogl, et al., Heavy-fermion behavior, crystalline electric field effects, and weak ferromagnetism in Sm Os 4 Sb 12, Phys. Rev. B—Condens. Matter Mater. Phys. 71 (10) (2005) 104402.

[41] A.L. Pope, B. Zawilski, T.M. Tritt, Description of removable sample mount apparatus for rapid thermal conductivity measurements, Cryogenics 41 (10) (2001) 725–731.